JACS
JOURNAL OF THE AMERICAN CHEMICAL SOCIETY
pubs.acs.org/JACS
Article

Tuning Defects in a Halide Double Perovskite with Pressure

Nathan R. Wolf, Adam Jaffe, Adam H. Slavney, Wendy L. Mao, Linn Leppert,* and Hemamala I. Karunadasa*

Cite This: J. Am. Chem. Soc. 2022, 144, 20763−20772
Read Online
ACCESS | Metrics & More | Article Recommendations | Supporting Information

ABSTRACT: Dopant defects in semiconductors can trap charge carriers or ionize to produce charge carriers—playing a critical role in electronic transport. Halide perovskites are a technologically important semiconductor family with a large pressure response. Yet, to our knowledge, the effect of high pressures on defects in halide perovskites has not been experimentally investigated. Here, we study the structural, optical, and electronic consequences of compressing the small-bandgap double perovskites Cs_2AgTlX_6 (X = Cl or Br) up to 56 GPa. Mild compression to 1.7 GPa increases the conductivity of $Cs_2AgTlBr_6$ by ca. 1 order of magnitude and decreases its bandgap from 0.94 to 0.7 eV. Subsequent compression yields complex optoelectronic behavior: the bandgap varies by 1.2 eV and conductivity ranges by a factor of 10^4. These conductivity changes cannot be explained by the evolving bandgap. Instead, they can be understood as tuning of the bromine vacancy defect with pressure—varying between a delocalized shallow defect state with a small ionization energy and a localized deep defect state with a large ionization energy. Activation energy measurements reveal that the shallow-to-deep defect transition occurs near 1.5 GPa, well before the cubic-to-tetragonal phase transition. An analysis of the orbital interactions in $Cs_2AgTlBr_6$ illustrates how the bromine vacancy weakens the adjacent Tl s−Br p antibonding interaction, driving the shallow-to-deep defect transition. Our orbital analysis leads us to propose that halogen vacancies are most likely to be shallow donors in halide double perovskites that have a conduction band derived from the octahedral metal's s orbitals.

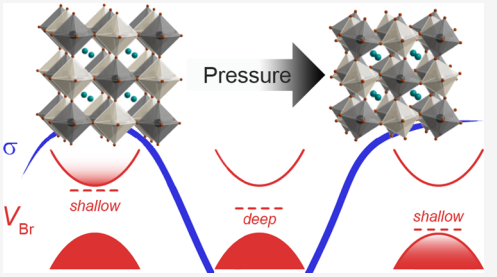

1. INTRODUCTION

Halide double perovskites such as the $A_2B^IB'^{III}X_6$ (A = monovalent cation, X = halide) elpasolites considerably expand on the compositional diversity of their $AB^{II}X_3$ parent structure.[1] This expansion offers access to diverse electronic structures, as exemplified by $Cs_2Ag^ITl^{III}X_6$ (X = Cl or Br), which exhibit bandgaps that are ca. 1 eV lower than those of other chloride or bromide perovskites, respectively.[2] The 0.95 eV bandgap of $Cs_2AgTlBr_6$ is among the smallest known for any halide perovskite. We previously found that $Cs_2AgTlBr_6$ spontaneously releases Br_2 gas, which dopes the material with electrons (eq 1a), evident from the increasing electronic conductivity that ranges from 10^{-5} to 10^{-2} S·cm^{-1} as a function of Br_2 loss.[2] This observation suggests that neutral bromine vacancies ($V_{Br}^{\times}$) ionize at room temperature to generate free electrons (e'_{CB}) in the conduction band (eq 1b),[3] with an ionization energy of ΔE_D, leading to an increased electron carrier concentration. The defect reaction equations below follow the Kröger−Vink notation,[3] where $Br_{Br}^{\times}$ represents the pristine lattice where a bromine atom occupies the bromine lattice position, $V_{Br}^{\times}$ represents a charge-neutral bromine vacancy, and $V_{Br}^{\bullet}$ represents a cationic bromine vacancy.

$$2Br_{Br}^{\times} \leftrightarrow Br_2(g) + 2V_{Br}^{\times} \quad (1a)$$

$$V_{Br}^{\times} \xleftrightarrow{\Delta E_D} V_{Br}^{\bullet} + e'_{CB} \quad (1b)$$

A point defect creates electronic states that are unique to the defect site, with an energy determined by local bonding and antibonding interactions. If the energy of the localized defect state is deep within the bandgap, charge carriers are readily trapped by the defect such that the defect is unlikely to be ionized, whereas if the defect is close to the band edges, it is more easily ionized. Alternatively, the localized defect state may have an energy that is outside the bandgap, commonly described as being resonant with the band. In this case, the charge carrier is not trapped in the localized electronic state and instead occupies the lower-energy electronic states resembling the band edge. However, the charge carrier can still be stabilized by the Coulombic attraction to the defect, similar to the stabilization of an electron by the nucleus in the hydrogen atom. This Coulombic attraction between charge carriers and defects generates partially delocalized, hydrogen-like electron states from which carriers can thermally promote into the fully delocalized, free carrier electronic states of the band edge. Thus, carriers in a deep defect occupy localized electronic states within the bandgap with a large ionization

Received: August 13, 2022
Published: November 7, 2022

https://doi.org/10.1021/jacs.2c08607
J. Am. Chem. Soc. 2022, 144, 20763−20772

energy, and carriers in a shallow defect, which accompanies a resonant state, occupy partially delocalized, hydrogen-like electronic states with a small ionization energy. Dopant defects are often distinguished solely by their ionization energy where shallow defects typically have an ionization energy less than 100 meV and deep defects have ionization energies larger than 100 meV.[4] However, the orbital composition and spatial localization of the defect electronic state are also important in the classification of a defect as shallow or deep (Figure 1A).

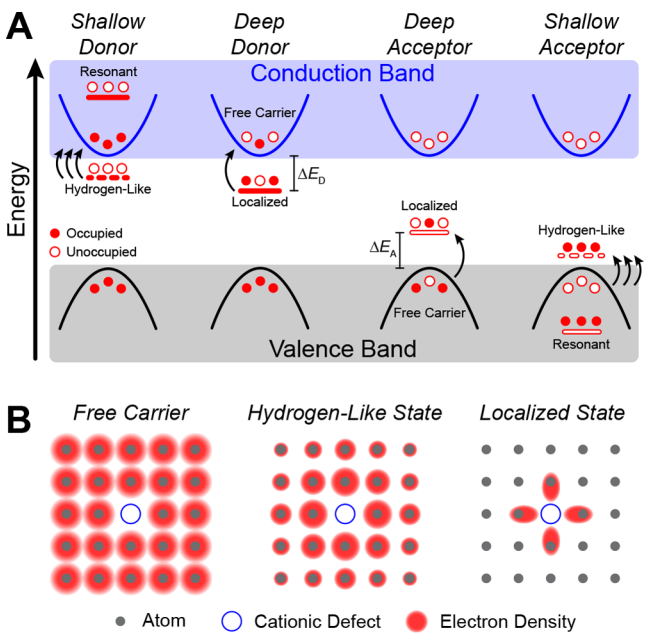

Figure 1. (A) Schematic of shallow donor/acceptor defects, which accompany localized defect states that are resonant with the band, and deep donor/acceptor defects that lie within the bandgap. The shallow donors have small ionization energies and contribute free carriers to the band edge by thermal ionization from hydrogen-like defect states (dotted red line). Deep donors/acceptors are only partially ionized due to their large ionization energy. (B) Spatial localization of defect electronic states depends on their character: free electrons in the conduction band are fully delocalized, electrons occupying a hydrogen-like state are partially localized near the defect, and electrons occupying deep defects are highly localized.

For example, the electron associated with a neutral bromine vacancy can be strongly bound to the defect (in the localized state with defect-derived orbitals), weakly bound to the defect (in the hydrogen-like state with orbitals derived from the band edges, modified by the Coulombic potential of the charged defect), or fully unbound by the defect (free carrier in band edge states).

The ionization energy of a defect (ΔE), illustrated in Figure 1A as ΔE_D for donors and ΔE_A for acceptors, is known to be tuned by compression for various materials,[5,6] prompting shallow defects to become deep defects,[7,8] or vice versa.[9] A shallow-to-deep defect transition occurs when a resonant state is driven into the bandgap by applying pressure.[6] In highly doped samples, the shallow-to-deep defect transition dramatically decreases the carrier concentration by several orders of magnitude. Furthermore, the different orbital character of shallow and deep defects impacts their sensitivity to high pressure. The ΔE of deep defects typically has a 100-fold larger dependence on pressure compared to the ΔE of shallow defects.[4,10] This difference in the rate of change of the ΔE with pressure occurs because the shallow hydrogen-like states are energetically derived from the nearby band edge and thus share its orbital composition, meaning that hydrogen-like states of shallow defects move in concert with the band edge. In addition, the energies of these delocalized shallow defects are dominated by long-range interactions that are less pressure-dependent. In contrast, deep defects involve localized wavefunctions that are more affected by interatomic distances (Figure 1B), making the ΔE of deep defects more sensitive to pressure. This allows for shallow and deep defects to be differentiated not only by the magnitude of their ΔE at ambient pressure but also by the pressure dependence of their ΔE.[4,10]

The high-pressure properties of halide perovskites have been studied since the 1970s,[11,12] revealing marked changes in the color, structure, and photophysical and transport properties of these soft semiconductors upon compression up to ca. 60 GPa (1 GPa ≈ 10,000 atm).[13−15] Due to the importance of dopant defects in semiconductor devices, defect energy levels have been closely studied at high pressure,[5,10,16−18] particularly for III−V semiconductors.[7,19−22] However, in high-pressure studies on halide perovskites, defects are most commonly discussed as shallow or deep traps for photoexcited carriers,[23−25] in contrast to their potential role as donor or acceptor dopants, which can produce free carriers.

To our knowledge, the high-pressure behavior of donor or acceptor dopants is experimentally unexplored in halide perovskites. Here, the low bandgap, high conductivity, and limited high-pressure amorphization of $Cs_2AgTlBr_6$ provide the novel opportunity to interrogate the relationships between compression-induced structural changes and corresponding orbital interactions that define the relative energies of the valence band maximum (VBM), conduction band minimum (CBM), and halogen vacancy defect state (V_X) in halide double perovskites. Using a combination of in situ high-pressure powder X-ray diffraction (PXRD), optical and vibrational spectroscopy, and electrical conductivity measurements in diamond anvil cells (DACs) coupled with first-principles density functional theory (DFT) calculations, we study the bromine vacancy defect (V_{Br}) in $Cs_2AgTlBr_6$ up to 56 GPa to establish a nuanced understanding of high-pressure defect behavior in halide double perovskites. For brevity, the discussion focuses on $Cs_2AgTlBr_6$ and reserves a detailed description of $Cs_2AgTlCl_6$ for the Supporting Information.

With initial compression up to 1.7 GPa, $Cs_2AgTlBr_6$ displays enhanced conductivity and a decreased bandgap relative to ambient pressure values. Upon further compression, however, complex electronic behavior arises. In contrast to other studies of halide perovskites under pressure, the changes in conductivity cannot be attributed to amorphization,[26,27] promotion of intrinsic carriers across the evolving bandgap,[28−31] or generation of disperse, partially occupied bands.[32−35] Instead, the high-pressure variations in conductivity are well described by the changing ΔE of a dopant defect, which we ascribe as V_{Br}. To better understand the impact of high-pressure structural changes on the transport properties, we then employ an orbital analysis to decompose the VBM, CBM, and V_{Br} electronic states into sets of bonding and antibonding orbital interactions. This orbital analysis points to the molecular interactions that drive the shallow-to-deep transition of the V_{Br} defect and allows us to propose that conduction bands formed from empty s orbitals will afford

https://doi.org/10.1021/jacs.2c08607
J. Am. Chem. Soc. 2022, 144, 20763−20772

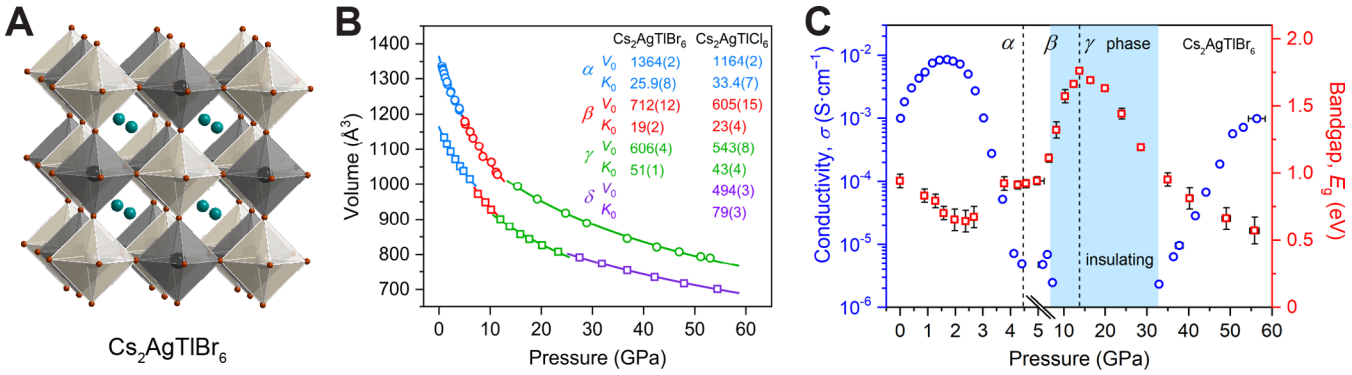

Figure 2. Structural and optoelectronic evolution of Cs_2AgTlX_6 (X = Cl or Br) with pressure. (A) Single-crystal X-ray structure of $Cs_2AgTlBr_6$ at ambient pressure (adapted from A. H. Slavney, L. Leppert, A. Saldivar Valdes, D. Bartesaghi, T. J. Savenije, J. B. Neaton, H. I. Karunadasa, Angew. Chem. Int. Ed. 2018, 57, 12765. Reproduced with permission). Teal, white, black, and brown spheres represent Cs, Ag, Tl, and Br atoms, respectively. (B) Unit cell compression of $Cs_2AgTlBr_6$ (circles) and $Cs_2AgTlCl_6$ (squares) and equation-of-state fits (solid lines). Initial volumes (V_0) in units of Å^3 and ambient-pressure bulk moduli (K_0) in units of GPa are listed for each phase. For clarity, unit cell volumes are doubled in the plots of the tetragonal β, γ, and δ phases. (C) Variable-pressure electronic conductivity, σ (blue circles), and bandgap, E_g (red squares), for $Cs_2AgTlBr_6$. The blue region denotes the lack of measurable conductivity between 7 and 33 GPa. Structural phase transitions are indicated above.

shallow V_{Br} defects in halide double perovskites—highly desirable for applications requiring mobile carriers.

2. RESULTS AND DISCUSSION

2.1. High-Pressure Structure, Bandgap, and Conductivity. All perovskites in this study were synthesized in solution and stored as powders or crystals for several days in closed vials at room temperature (see the Supporting Information). Thus, we expect appreciable n-type doping of $Cs_2AgTlBr_6$ by spontaneous halogen degassing.[2] After the sample is loaded and sealed into a DAC for conductivity experiments, this self-doping mechanism is presumably halted by the lack of headspace, thereby establishing a fixed doping concentration. The observed high conductivity and small activation energy of conduction, which is significantly lower than the bandgap energy, are characteristic of electronic doping in $Cs_2AgTlBr_6$.

Upon compression, $Cs_2AgTlBr_6$ maintains its $Fm\bar{3}m$ cubic symmetry up to 4.0 GPa (Figure 2A,B). The measured pressure−volume relationship was fit to a second-order Birch−Murnaghan equation of state to determine the ambient-pressure bulk modulus K_0 = 25.9(8) GPa for the α phase (Figure 2B). The bandgap decreases from 0.94(5) eV at ca. 0 GPa to 0.64(8) eV at 2.4 GPa (Figure 2C) consistent with enhanced band dispersion through better orbital overlap induced by shorter metal−halide distances. Compression to 2.4 GPa also yields a more gradual absorption edge (Figure S1A), which may be related to increased band dispersion and the symmetry-forbidden nature of the direct bandgap.[2] The conductivity rises by nearly an order of magnitude in this lower-pressure regime, from 9.9×10^{-4} S·cm^{-1} at 0.03 GPa to 8.5×10^{-3} S·cm^{-1} at 1.7 GPa.

Between 2.7 and 3.8 GPa, the bandgap sharply increases from 0.67(8) to 0.92(5) eV. However, accurate determination of the bandgap between 2.7 and 3.8 GPa is inhibited by the phase change in KBr, which begins near 2.3 GPa and causes irregular opacity between the reference and sample scans. Thus, we conclude that the bandgap increase begins somewhere between 2.7 and 3.8 GPa, eventually reaching a maximum bandgap value of 1.76(1) eV at 14 GPa (Figure S1B). This increasing bandgap is accompanied by a steep decrease in conductivity from 8.0×10^{-3} S·cm^{-1} at 1.9 GPa to 2.5×10^{-6} S·cm^{-1} at 7.3 GPa, after which no measurable conductivity is observed until 33 GPa (Figure 2C). Between 4.0 and 5.1 GPa, $Cs_2AgTlBr_6$ undergoes a phase transformation characterized by a splitting of diffraction peaks, a reduction in peak intensities, and an increase in amorphous background signal (Figure S2). We index this high-pressure β phase to the tetragonal space group $I4/m$, which is a common high-pressure double-perovskite phase[36,37] and is observed in $Cs_2AgBiBr_6$ at 30 K at ambient pressure.[38] Notably, the higher-pressure β phase (K_0 = 19(2) GPa) is ca. 20% more compressible than the lower-pressure α phase. The $I4/m$ symmetry of the β phase enables octahedral rotations in the ab-plane, which dominate volume reduction in this phase and thereby enhance the compressibility.

In the highest-pressure regime studied, the bandgap of $Cs_2AgTlBr_6$ decreases monotonically from 1.76(1) eV at 14 GPa to 0.6(1) eV at 56 GPa (Figure S1C). Conductivity reemerges above 33 GPa and continues to increase up to a value of 9.8×10^{-4} S·cm^{-1} at 56 GPa. Above 15 GPa, there is a ca. 40% decrease in lattice compressibility consistent with a second-order, isostructural transition to a higher-pressure γ phase with $I4/m$ symmetry (K_0 = 51(1) GPa). The lower compressibility of the higher-pressure γ phase relative to the β phase suggests that further octahedral rotations become limited above 15 GPa and bond compression returns as the primary means of lattice compression (see high-pressure structures in Section 2.2). Both the α-to-β phase change near 4 GPa and the β-to-γ phase change near 15 GPa coincide with the turning points of the bandgap trends. Thus, octahedral rotation in the β phase (5.1−11 GPa) increases the bandgap, whereas bond compression in the α phase (0−4.0 GPa) and γ phase (15−53 GPa) lowers the bandgap (Figure 2C). High-pressure Raman measurements support the phase changes observed by PXRD (Figure S3).

The high-pressure behavior of $Cs_2AgTlCl_6$ closely resembles that of $Cs_2AgTlBr_6$, albeit with a high-pressure δ phase. However, the magnitude of changes in bandgap of $Cs_2AgTlCl_6$ is smaller than that of the bromide analog, which may be attributed to the less diffuse Cl p states, similar to the differences between two-dimensional (2D) Cu−Cl and Cu−Br perovskites.[33] Therefore, the high-pressure optoelectronic properties of $Cs_2AgTlBr_6$ were investigated in more detail.

https://doi.org/10.1021/jacs.2c08607
J. Am. Chem. Soc. 2022, 144, 20763−20772

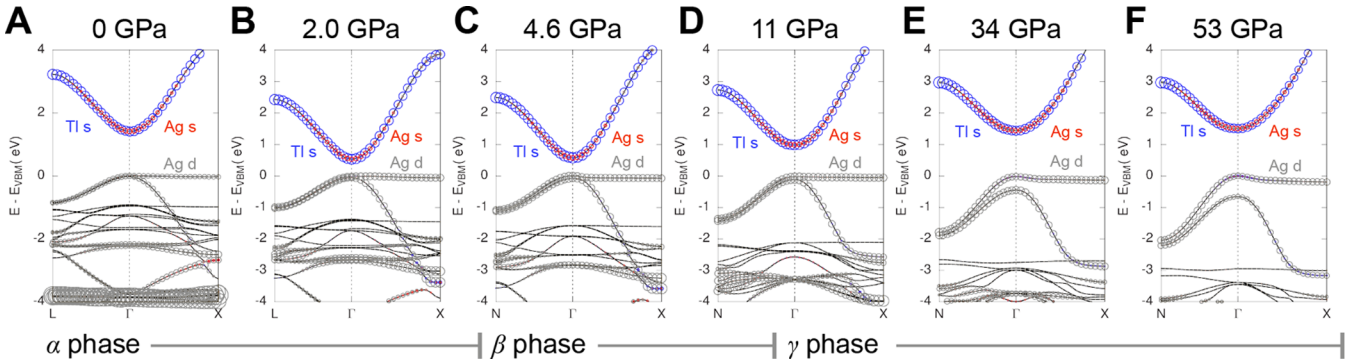

Figure 3. Band structures of $Cs_2AgTlBr_6$ at high pressure. Calculations were performed with DFT-PBE*x*, where x = 35% exact exchange. Atomic orbital contributions from Ag d, Ag s, and Tl s are illustrated as gray, red, and blue circles, respectively. Corresponding structural phases are indicated below.

2.2. High-Pressure Band Structures. Pressure is known to tune bandgap character much like compositional alloying.[39−41] To better understand the impact of lattice compression on the orbital composition and dispersion of the band edges in $Cs_2AgTlBr_6$, we calculated electronic band structures at 0, 2.0, 4.6, 11, 34, and 53 GPa using first-principles DFT calculations with a global hybrid functional incorporating 35% of exact exchange (PBE*x*; see the Supporting Information). High-pressure structures were derived by optimizing atom positions from an initial $Fm\bar{3}m$ (α phase) or $I4/m$ (β and γ phases) unit cell with experimentally derived lattice parameters. These calculated high-pressure crystal structures support our interpretation of the interplay between bond compression and octahedral tilting (Figure S9). The bandgap remains direct at Γ and the orbital character of the band edges is maintained up to a pressure of 34 GPa (Figures 3 and S10). The VBM is derived from Br p and Ag d orbitals and the CBM is derived from Tl s, Ag s, and Br p orbitals. Calculations at 53 GPa suggest a band inversion, with Tl s character at the VBM and Ag d character at the CBM, indicative of topologically nontrivial behavior (see the Supporting Information).

The calculated high-pressure electron and hole effective masses (m_e* and m_h*, respectively) reflect the structural changes occurring in $Cs_2AgTlBr_6$ upon compression. In the cubic α phase, the shortening of bonds enhances band dispersion and decreases the electron effective mass from 0.18 m_0 at ambient pressure to 0.15 m_0 at 2.0 GPa, where m_0 is the mass of a free electron (Figure S11). Notably, after the phase change to tetragonal symmetry, the electron effective mass remains at 0.15 m_0 at 4.6 GPa, indicating that the dramatic decrease in conductivity, starting near 2 GPa, cannot be attributed to a decrease in mobility in the α or β phase. The electron effective mass increases to 0.24 m_0 at 11 GPa and 0.44 m_0 at 34 GPa due to further octahedral rotations that decrease the conduction band dispersion. In addition, the hole effective mass decreases steadily from 0.41 m_0 at ambient pressure to 0.19 m_0 at 34 GPa.

Qualitative comparisons of band dispersion across the series of high-pressure band structures illustrate the dominant changes in each pressure regime (Figure 3). In the cubic α phase, where lattice compression occurs solely from bond compression, both the valence band and conduction band become more disperse from ambient pressure to 2.0 GPa. In the tetragonal β phase from 4.6 to 11 GPa, the dispersion of the conduction band decreases considerably while the dispersion of the valence band is somewhat enhanced. This suggests that the increase in bandgap in the β phase, coinciding with octahedral rotations, is caused by an increase in energy of the CBM as the conduction band becomes less disperse. Finally, the comparison of band structures at 11, 34, and 53 GPa demonstrates that increasing pressure in the tetragonal γ phase enhances the band dispersion of the valence band while concurrently decreasing the band dispersion of the conduction band, suggesting that the decreasing bandgap in the γ phase is caused by a rise in energy of the VBM. The qualitative trends discussed above are supported by a quantitative analysis of the bandwidths of the valence band and conduction band between high-symmetry k-points (Figure S12) and explained by the orbital analysis presented in Section 2.5.

2.3. High-Pressure Tuning of V_{Br}. As previously discussed, the high-pressure changes in the electrical conductivity of $Cs_2AgTlBr_6$ cannot be attributed to intrinsic carriers, communication between partially occupied orbitals, changes in carrier mobility, or changes in bandgap orbital composition. Thus, we attribute the trends in conductivity to changes in the ionization energy (ΔE) of the dopant defect: V_{Br}. Previous work at ambient pressure demonstrated that $Cs_2AgTlBr_6$ is n-type doped by Br_2 loss,[2] thereby supporting the assignment of n-type conductivity below 7 GPa. After conductivity reemerges above 33 GPa, however, the n-type or p-type character of the material cannot be conclusively assigned. Band structure calculations in the γ phase show that the dominant change in electronic structure is the increasing dispersion of the valence band, leading us to interpret that the approach of the VBM toward an acceptor dopant generates p-type conductivity above 33 GPa. The possibility and implications of n-type conductivity above 33 GPa are discussed in the Supporting Information.

Variable-temperature conductivity measurements in the α phase of $Cs_2AgTlBr_6$ at 0.10(5), 0.77(8), 1.6(1), and 2.3(2) GPa reveal activation energies of conduction (E_{act}) of 129(6), 134(4), 174(6), and 340(2) meV, respectively (Figures 4 and S13). Because these values are significantly smaller than the bandgap at these pressures, the E_{act} values are assigned to the thermal excitation of electrons from V_{Br} to the CBM, which constitutes a transition between the neutral and cationic charge states of V_{Br}. When conductivity is limited by the thermal promotion of carriers from a defect, E_{act} is related to the defect ionization energy (ΔE_D) such that $\Delta E_D \approx 2E_{act}$.[42]

The small change in E_{act} between 0.10(5) and 0.77(8) GPa signifies that V_{Br} is a shallow donor at near ambient pressures

https://doi.org/10.1021/jacs.2c08607
J. Am. Chem. Soc. 2022, 144, 20763−20772

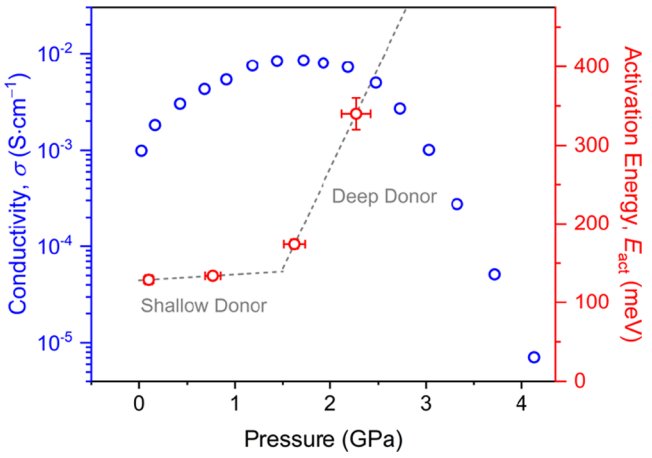

Figure 4. Electrical conductivity, σ (blue circles), and activation energy, E_{act} (red circles), of $Cs_2AgTlBr_6$ in the cubic α phase. The shallow-to-deep defect transition is illustrated by a steeper pressure dependence of the activation energy, which occurs near 1.5 GPa. Dotted lines are a guide to the eye.

and moves in concert with the CBM upon compression. Using DFT-PBEx with x = 35% exact exchange, the static dielectric constant of $Cs_2AgTlBr_6$ at ambient pressure is $3.44\varepsilon_0$ (calculated within the independent-particle approximation; ε_0 = permittivity of free space). By applying the effective mass approximation for a hydrogen-like shallow defect,[43,44] the predicted value of ΔE_D = 210 meV is in good agreement with the experimental value of $\Delta E_D \approx 2E_{act}$ = 258(16) meV at 0.10(5) GPa.

The experimental E_{act} increases sharply between 1.6(1) and 2.3(2) GPa, consistent with the behavior of a deep defect, which moves independently of a band edge with pressure. The observed change in slope suggests that the shallow-to-deep defect transition occurs near 1.5 GPa (Figure 4). Importantly, the sudden upturn of E_{act} also coincides with the turning point of the electrical conductivity. The conductivity decreases rapidly after ~2 GPa even though the calculated m_e* remains unchanged from 2.0 to 4.6 GPa. We therefore assign this decrease in conductivity to a decrease in electron carrier concentration due to the higher ΔE_D of V_{Br} as a deep defect.

We interpret the return of measurable conductivity above 33 GPa as the approach of an acceptor state to the VBM, giving rise to p-type conductivity. Although other defects are possible, most likely this acceptor state corresponds to the ionization of a neutral bromine vacancy ($V_{Br}^{\times}$) to generate a free hole ($h_{VB}^{\bullet}$) in the valence band and an anionic bromine vacancy (V_{Br}'), as shown in eq 2. Here, the ionization energy of the acceptor state is ΔE_A.

$$V_{Br}^{\times} \overset{\Delta E_A}{\longleftrightarrow} V_{Br}' + h_{VB}^{\bullet} \quad (2)$$

The E_{act} values in the γ phase at 48 and 58 GPa were measured to be 177(5) and 151(2) meV, respectively (Figure S14). This relatively small change in E_{act} suggests that the acceptor defect state above 48 GPa is shallow, meaning that a deep-to-shallow acceptor transition likely occurs between 33 and 48 GPa.

2.4. Atomic and Electronic Structure of V_{Br}. Detailed DFT calculations on halide perovskites at ambient pressure show that an across-vacancy bonding interaction stabilizes V_X and is responsible for significant B-site atom relaxation toward the vacancy for neutral and anionic halogen vacancies,[45,46] although this observation is subject to debate.[47] The across-vacancy bonding interaction does not similarly stabilize the cationic V_X state because it is unoccupied by electrons, thus removing the driving force for neighboring B sites to form a bond. Because the donor and acceptor behavior of V_X corresponds to equilibria between defect charge states (eqs 1b and 2), energetic stabilization of neutral and anionic halogen vacancies leads to a deeper donor transition (larger ΔE_D) and a shallower acceptor transition (smaller ΔE_A).

To uncover the high-pressure atomic structure of V_{Br} in $Cs_2AgTlBr_6$, DFT structural calculations were performed on 320-atom (cubic) or 360-atom (tetragonal) supercells at 0, 2.0, and 4.6 GPa with V_{Br} in either the cationic, neutral, or anionic charge state (see the Supporting Information). The charge state of V_{Br} did not strongly affect the positions of the atoms around the defect, in contrast to previous reports on halide perovskites at ambient pressure (Figure S15).[45−49] In the local structure of cationic, neutral, and anionic V_{Br}, neighboring Ag and Tl atoms relax away from the site of the vacancy at ambient pressure (Figure S16). This ambient pressure B-site cation relaxation away from the vacancy site can be understood as stemming from the loss of the Coulombic attraction to the formerly anionic bromide site (since the electron is not localized at the bromide site even in the anionic V_{Br}'). However, in the 2.0 GPa calculations, the Ag−Tl distances in the pristine structure and across the vacancy are similar. At 4.6 GPa, the observed Ag−Tl distances across the vacancy (4.87−5.05 Å) are shorter than the Ag−Tl distance in the pristine material at the same pressure (5.29 Å). These results demonstrate that B-sites neighboring the V_{Br} defect are driven toward the vacancy space with increasing pressure. However, the across-vacancy Ag−Tl distances at 4.6 GPa constitute a 5−8% contraction relative to the pristine structure at the same pressure, in contrast to the much larger ca. 30% contraction of across-vacancy Pb−Pb distances that are reported in cases where strong across-vacancy Pb−Pb orbital interactions are calculated in lead-halide perovskites.[23,49] Considering that the across-vacancy Ag−Tl distances are relatively large and weakly dependent on the V_{Br} charge state, it is unlikely that there is a strong across-vacancy Ag−Tl orbital interaction in $Cs_2AgTlBr_6$ at pressures below 4.6 GPa. The absence of an across-vacancy Ag−Tl orbital interaction may be due to the spherical Tl s and Ag s orbitals being less directed at the vacancy in contrast to the Pb p orbitals.

Next, the electronic structure of the neutral V_{Br} defect was calculated for the ambient pressure structure. The impact of V_{Br} on the electronic structure is revealed by comparing the density of states at the Γ point for $Cs_2AgTlBr_6$ with and without a neutral V_{Br}. The presence of V_{Br} generates an unfilled, spatially localized resonant state in the conduction band that is largely localized on the Tl site neighboring the V_{Br} defect (Figure S17) and results in an unpaired electron residing in a CBM-derived, delocalized electronic state. This is consistent with the understanding that shallow hydrogen-like donor defect states arise when a localized donor defect state is resonant with the conduction band (Figure 1A). The shallow-to-deep defect transition near 1.5 GPa is caused by the high-pressure stabilization of this localized neutral V_{Br} state relative to the CBM such that eq 1b favors the reactants and ΔE_D increases.

2.5. Orbital Analysis of the CBM, VBM, and V_{Br} States. The high-pressure bandgap trends are determined by relative changes in the CBM and VBM energies. On the other hand, the high-pressure conductivity trends are determined by

https://doi.org/10.1021/jacs.2c08607
J. Am. Chem. Soc. 2022, 144, 20763−20772

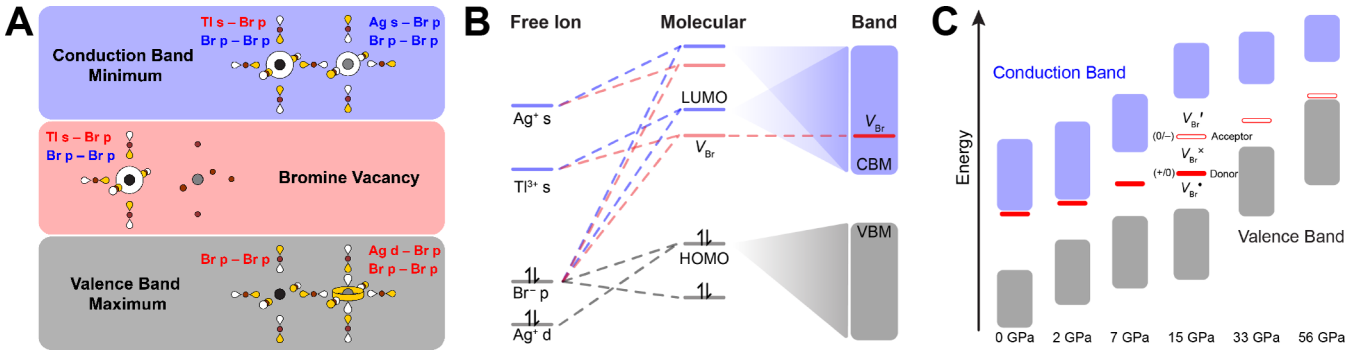

Figure 5. Orbital interactions determine the energy positions of the CBM, VBM, and V_{Br} at high pressures. (A) Illustration of orbital interactions defining the CBM, VBM, and V_{Br} electronic states in $Cs_2AgTlBr_6$. Tl and Ag atoms are represented in black and gray, respectively. Positive and negative phases of orbitals are illustrated in white and yellow. Antibonding and bonding orbital interactions are noted in red and blue font, respectively. (B) Atomic orbitals of free ions interact to form molecular orbitals that determine the CBM, VBM, and V_{Br} electronic states. Band dispersion in the CBM helps determine the relative position of the CBM and V_{Br}. See Figure S18 for a detailed view. (C) Graphical summary of changes in relative energy of the CBM, VBM, and V_{Br} donor and acceptor transitions in $Cs_2AgTlBr_6$ at high pressures. The donor transition (+/0) indicates the Fermi energy at which the cationic $V_{Br}^{\bullet}$ and neutral $V_{Br}^{\times}$ states have equal concentrations, and the acceptor transition (0/−) indicates the Fermi energy at which the neutral $V_{Br}^{\times}$ and anionic V_{Br}' states have equal concentrations.

changes in ΔE_D in the n-type regime below 7 GPa and changes in ΔE_A in the p-type regime above 33 GPa. In the absence of large structural changes between charge states of V_{Br}, ΔE_D of the deep donor transition can be approximated as the relative energy difference between the CBM and neutral V_{Br} state, and ΔE_A of the deep acceptor transition can be approximated as the relative energy difference between the VBM and anionic V_{Br} state. By analyzing the orbital interactions that compose the CBM, VBM, and V_{Br} states (Figure S18), the observed changes in bandgap and conductivity can be understood with respect to structural changes induced by pressure.

First, we obtain the orbital composition of the VBM using our previously described molecular orbital approach that assesses the interactions between symmetry-adapted linear combinations of halogen p orbitals with B-site metal atomic orbitals of compatible symmetry.[50] This methodology for double perovskites reveals that the energy of a given band will first be determined by a dominant orbital interaction at one of the B sites, which contributes to the band at all points in reciprocal space (i.e., at all k points). The curvature of the band then arises from applying translational symmetry, which modifies the bonding and antibonding interactions across the nondominant B′ site. Here metal−halide σ bonds exert the largest effect on band dispersion, followed by weaker halide−halide interactions between halides that are at 90° angles with respect to each other. Our molecular orbital analysis is validated by DFT electron density maps of $Cs_2AgTlBr_6$ (Figure S23).

For the valence band of $Cs_2AgTlBr_6$, the dominant orbital interaction is a σ^* antibonding interaction of Ag $d_{x^2-y^2}$ and d_{z^2} orbitals with Br p E_g orbitals within the $[AgBr_6]^{5-}$ octahedra (Figure 5A). Because the filled Tl 5d orbitals are too low in energy to strongly contribute to the VBM, translational symmetry generates the VBM at Γ and X due to a maximized antibonding interaction of Br p orbitals that are oriented at 90° angles with respect to each other in the $[TlBr_6]^{3-}$ octahedra.[50] Metal−halide bond compression in the α phase enhances both these antibonding interactions such that the VBM rises in energy. In the β and γ phases, the 2-fold degeneracy of the VBM is lost (Figure 3), leading to a VBM at Γ that is primarily composed of Ag d_{z^2} orbitals (see discussion in the Supporting Information). Octahedral tilting in the ab-plane weakens band dispersion of the Ag $d_{x^2-y^2}$ orbital-derived band while having less impact on the Ag d_{z^2} orbital-derived band because the Ag d_{z^2} orbitals interact most strongly with the axial halides along the c-axis, which maintain B−X−B bond angles of 180° (Figure S24). This explains why the band dispersion of the d_{z^2} orbital-derived VBM increases monotonically with pressure and is insensitive to octahedral tilting in the ab-plane. In the γ phase above 11 GPa, bond compression returns as the major mode of volume reduction, which significantly raises the energy of the VBM because bond compression has the additive effect of enhancing both the Ag d−Br p and the Br p−Br p antibonding interactions.

Next, for the conduction band of $Cs_2AgTlBr_6$, the dominant orbital interaction is an antibonding interaction of Tl s with Br p A_{1g} orbitals in the $[TlBr_6]^{3-}$ octahedra (Figure 5A). By applying translational symmetry, the CBM appears at Γ due to two bonding interactions: (1) a bonding interaction between Ag s orbitals and Br p A_{1g} orbitals in the $[AgBr_6]^{5-}$ octahedra, which introduces Ag s character into the CBM at Γ and (2) a bonding interaction between Br p orbitals that are oriented at 90° angles with respect to each other in the $[AgBr_6]^{5-}$ octahedra. Again, a similar Br p−Br p bonding interaction occurs in the $[TlBr_6]^{3-}$ octahedra, yet it is unchanged by translational symmetry because the dominant Tl s−Br p interaction necessitates A_{1g} symmetry of the Br p orbitals in the $[TlBr_6]^{3-}$ octahedra. In the α phase, metal−halide bond compression enhances the antibonding Tl s−Br p interaction and the bonding Ag s−Br p and Br p−Br p interactions, which have competing effects on the energy of the CBM. The enhanced bonding interactions in the $[AgBr_6]^{5-}$ octahedra increase band dispersion to lower the energy of the CBM, whereas the dominant Tl s−Br p antibonding interaction raises the energy of the entire conduction band. These counteracting interactions cause a weaker pressure dependence of the energy of the CBM in the α phase, which together with the rising energy of the VBM, leads to the observed decrease in bandgap energy in the α phase. The bandgap increase in the β phase is largely due to a rise in the energy of the CBM because octahedral tilting weakens the bonding interactions of the CBM. This interpretation is supported by the steadily decreasing dispersion in the conduction band from 4.6 to 53 GPa (Figures 3 and S12). Despite the dominance of bond

https://doi.org/10.1021/jacs.2c08607
J. Am. Chem. Soc. 2022, 144, 20763−20772

compression in the γ phase, the conduction band continues to become less dispersed because of the higher sensitivity to the ongoing octahedral tilting.

Third, we consider the orbital composition of the localized neutral V_{Br} state, which is resonant with the conduction band below 1.5 GPa. Generation of a neutral V_{Br} transforms the neighboring O_h $[AgBr_6]^{5-}$ and $[TlBr_6]^{3-}$ octahedra into C_{4v} $[AgBr_5]^{4-}$ and $[TlBr_5]^{2-}$ square pyramidal units, respectively, where a supplementary donated electron from the defect must occupy the lowest unoccupied molecular orbital (LUMO) of either $[AgBr_5]^{4-}$ or $[TlBr_5]^{2-}$ units, which have the same valence electronic configuration. The LUMO of both square pyramidal units is an antibonding interaction of the B-site s orbital with one set of the Br p A_1 orbitals (Figure S18B, see discussion in the Supporting Information). The smaller negative charge and more diffuse orbitals of $[TlBr_5]^{2-}$ compared to $[AgBr_5]^{4-}$ suggest that $[TlBr_5]^{2-}$ has the lower-energy LUMO, explaining why the DFT calculations showed a resonant defect state localized on the Tl atom neighboring V_{Br} (Figure S17). The orbital composition of V_{Br} is thus an antibonding Tl s−Br p interaction and a weaker bonding Br p−Br p interaction in the C_{4v} $[TlBr_5]^{2-}$ unit (Figure 5A). Our analysis shows that the neutral V_{Br} state is indeed resonant with the conduction band at ambient pressure because the additional bonding Ag s−Br p and Br p−Br p interactions of the O_h $[AgBr_6]^{3-}$ units that compose the CBM lower the energy of the CBM below the neutral V_{Br} state. This lowering of the CBM arises from the delocalization of the conduction band wavefunction, which provides band dispersion that does not apply to the localized V_{Br} state (Figure 5B). The antibonding Tl s−Br p interaction is the dominant orbital interaction of both the CBM and the V_{Br} state. This antibonding interaction is five-coordinate for V_{Br} and six-coordinate for the CBM, indicating that V_{Br} has the weaker Tl s−Br p interaction between the two. With increasing pressure, the differing strength of the antibonding Tl s−Br p interactions will cause the CBM to rise faster than the neutral V_{Br} state, resulting in V_{Br} eventually entering the bandgap, which drives the shallow-to-deep defect transition we observe near 1.5 GPa.

As previously discussed, an additional bonding interaction between the Tl s and Ag s orbitals may arise across the halogen vacancy, particularly at high pressures. Indeed, a computational investigation of $FA_{0.75}Cs_{0.25}PbI_3$ illustrates a shallow-to-deep defect transition of the V_I defect below 2 GPa caused by an across-vacancy Pb−Pb bond.[23] Our atom relaxations of V_{Br} demonstrate that high pressure drives the neighboring B-site cations toward the vacancy, but no indication of an across-vacancy Ag−Tl orbital interaction is found up to 4.6 GPa (Figure S16). Thus, we discard the importance of the across-vacancy Tl s−Ag s interaction as a cause for the shallow-to-deep defect transition near 1.5 GPa. At pressures higher than 4.6 GPa, this across-vacancy Tl s−Ag s interaction may be more relevant, potentially being responsible for stabilizing the anionic V_{Br} state and decreasing ΔE_A. Our qualitative interpretation of the high-pressure changes in relative energy of the VBM, CBM, and V_{Br} states is graphically summarized in Figure 5C. Here, the energy position of the V_{Br} donor transition represents the Fermi energy at which the cationic $V_{Br}^{\bullet}$ and neutral $V_{Br}^{\times}$ states have equivalent formation energies and thus equal concentrations. Likewise, the V_{Br} acceptor transition is positioned at the Fermi energy at which the neutral $V_{Br}^{\times}$ and anionic V_{Br}' states have equivalent formation energies and concentrations.

2.6. Designing Halogen Vacancies as Shallow Donors. Finally, design principles that may afford shallow halogen vacancies in halide double perovskites are highly desirable, in analogy to discussions of shallow oxygen vacancies in oxides.[51,52] Semiconductors generally achieve higher performance (e.g., long carrier lifetime and diffusion length) when their lattice imperfections are shallow defects that generate electronic states near the band edges or within the bands. Defects in lead-halide perovskites are typically viewed as nonradiative recombination sites for photogenerated charge carriers,[53] and the materials' tolerance to defects formed during synthesis has been linked to the shallow nature of these defects. Additionally, shallow defects enable opportunities for electrical doping of a semiconductor.[54] However, in contrast to oxide perovskites, electrically doping most halide perovskites remains a challenge, in part due to defect compensation during synthesis.[55] Halogen exchange as reported in $(CH_3NH_3)PbI_3$[56] and $Cs_2AgTlBr_6$[2] tunes the doping in halide perovskites by changing the halogen vacancy concentration after synthesis.

The shallow nature of halogen vacancies in lead-halide perovskites is widely considered to originate from the fact that dangling Pb p orbitals are higher in energy than the CBM.[57,58] However, calculations suggest that bonding interactions between Pb atoms across a halogen vacancy can generate a deep halogen vacancy state.[45,46] Shallow halogen vacancies can be pursued in double perovskites by designing either a low-energy CBM or a high-energy V_X state. First, a large degree of band dispersion in the conduction band will lower the energy of the CBM. This band dispersion is best accomplished by including two B-site cations with the same electronic configuration, e.g., $Cs_2AgTlBr_6$[2] or $(CH_3NH_3)_2TlBiBr_6$.[59] The larger conduction band dispersion of $Cs_2AgTlBr_6$[60] compared to $(CH_3NH_3)_2TlBiBr_6$[59] suggests that an s-orbital-derived CBM is more promising to yield shallow halogen vacancies. However, this approach of matching B-site orbitals in the conduction band is limited because the isolation of compounds such as $Cs_2AgInBr_6$[61] and Cs_2InBiX_6[62] (X = Cl or Br) remains synthetically challenging.

Alternatively, a stronger antibonding interaction of the $[BX_5]^{n-}$ LUMO will increase the energy of the V_X state, making it more likely to be a shallow donor. For a V_X state arising from an s-orbital-derived CBM, a halogen vacancy removes one of the six halogen p orbitals that interact with an empty B-site s orbital, somewhat weakening the antibonding interaction. However, for a V_X state arising from a p-orbital-derived CBM, the halogen vacancy, which reduces the coordination symmetry to C_{4v} symmetry, breaks the 3-fold degeneracy of B-site p orbitals. Thus, the halogen vacancy removes one of just two halogen atoms that interact with an empty p orbital at the B site, significantly weakening the antibonding interaction that gives rise to the V_X state (Figure S19). In addition, compared to s orbitals, p orbitals are better oriented to generate a bonding interaction across the vacancy, potentially lowering the energy of the V_X state.[48] Taken together, both these considerations of band dispersion and V_X orbital antibonding strength may explain why shallow V_X defects have, to our knowledge, only been experimentally observed for double perovskites with CBMs composed of empty s orbitals: e.g., $Cs_2AgTlBr_6$ and Cs_2SnI_6.[2,63] Additionally, computational studies of halogen vacancies in double perovskites generally, but not always,[64] find that V_x is shallow when B′ = In^{3+} but deep when B′ = Bi^{3+}.[48,65−67] The lower formation energy of halogen vacancies in double perovskites

https://doi.org/10.1021/jacs.2c08607
J. Am. Chem. Soc. 2022, 144, 20763−20772

with B′ = In^{3+} compared to B′ = Bi^{3+} has been previously attributed to s-orbital character in the CBM.[68] In light of the synthetic challenges of discovering novel double perovskites with s-orbital-derived CBMs, and the dramatic effects of dilute impurity alloying seen in these materials,[69,70] it may be sufficient to engineer solely the local orbital structure of a halogen vacancy to generate a high-energy, resonant V_x state that acts as a shallow donor. For example, a halide double perovskite may be doped with a B-site cation with a high-energy empty s orbital (i.e., Sc^{3+}, Y^{3+}) that yields high-energy V_x states with neighboring halogen vacancies without modifying the band edge states, resulting in n-type doping from electrons that relax from the high-energy V_x state to the conduction band as delocalized free electrons. This strategy involves homovalent doping, which avoids charge-compensating defects that are expected in heterovalent doping (e.g., trivalent rare-earth dopants that yield shallow defect states in lead perovskites).[71]

3. CONCLUSIONS

We show that the small-bandgap halide double perovskites Cs_2AgTlX_6 (X = Cl or Br) are highly sensitive to compression. At only 1.7 GPa, $Cs_2AgTlBr_6$ exhibits a ca. 10-fold enhanced conductivity and bandgap of 0.7 eV. Upon further compression, both the bromide and chloride congeners show substantial bandgap widening followed by bandgap reduction. The bandgap evolution can be understood through the interplay of metal−halide bond compression and interoctahedral rotations, each of which dominates in distinct pressure regimes. In $Cs_2AgTlBr_6$, octahedral rotations widen the bandgap in the β phase (5.1−11 GPa) by decreasing the dispersion of the conduction band, whereas bandgap narrowing in the α phase (0−4.0 GPa) and γ phase (15−53 GPa) results from metal−halide bond compression. The high-pressure conductivity, however, is not dictated by the bandgap magnitude and is instead governed by the pressure-tuning of the energy of the V_{Br} state with respect to the band edges. A shallow-to-deep defect transition occurs near 1.5 GPa, prompting a dramatic decrease in free carriers that decreases conductivity by at least 4 orders of magnitude. The return of measurable conductivity above ca. 30 GPa in the γ phase, proposed to be p-type, is caused by bond compression, which raises the energy of the VBM to approach the V_{Br} acceptor transition. An orbital analysis of the V_{Br} state illustrates that the antibonding Tl s−Br p interaction is weakened by the loss of a bromide ligand, leading to the pressure-induced shallow-to-deep defect transition as the conduction band rises in energy faster than the neutral V_{Br} state upon compression. The study of shallow-to-deep defect transitions in $Cs_2AgTlBr_6$ at high pressure has led us to recognize that shallow V_X donors are most likely in halide double perovskites with CBMs derived from empty s orbitals. We further propose that doping double perovskites with B-site cations containing high-energy empty s orbitals will generate shallow donor defects by raising the energy of the neutral V_X donor state above the CBM. Thus, by tracking the structural and electronic evolution of $Cs_2AgTlBr_6$ at high pressure, we can elucidate the orbital and atomic character of V_{Br} to lay the groundwork for the rational electronic doping of double perovskites.

■ ASSOCIATED CONTENT

Supporting Information

The Supporting Information is available free of charge at https://pubs.acs.org/doi/10.1021/jacs.2c08607.

Experimental and computational details, diffraction patterns, spectra, and supplemental discussion (PDF)

■ AUTHOR INFORMATION

Corresponding Authors

Linn Leppert − *MESA+ Institute for Nanotechnology, University of Twente, 7500 AE Enschede, The Netherlands; Institute of Physics, University of Bayreuth, 95440 Bayreuth, Germany;* orcid.org/0000-0002-4361-4382; Email: l.leppert@utwente.nl

Hemamala I. Karunadasa − *Department of Chemistry, Stanford University, Stanford, California 94305, United States; Stanford Institute for Materials and Energy Sciences, SLAC National Accelerator Laboratory, Menlo Park, California 94025, United States;* orcid.org/0000-0003-4949-8068; Email: hemamala@stanford.edu

Authors

Nathan R. Wolf − *Department of Chemistry, Stanford University, Stanford, California 94305, United States*

Adam Jaffe − *Department of Chemistry, Stanford University, Stanford, California 94305, United States;* Present Address: Department of Chemistry and Biochemistry, University of Notre Dame, Notre Dame, Indiana 46556, United States; orcid.org/0000-0002-9886-0249

Adam H. Slavney − *Department of Chemistry, Stanford University, Stanford, California 94305, United States*

Wendy L. Mao − *Department of Geological Sciences, Stanford University, Stanford, California 94305, United States; Stanford Institute for Materials and Energy Sciences, SLAC National Accelerator Laboratory, Menlo Park, California 94025, United States*

Complete contact information is available at: https://pubs.acs.org/10.1021/jacs.2c08607

Notes

The authors declare no competing financial interest.

■ ACKNOWLEDGMENTS

This work was supported by the Department of Energy, Office of Basic Energy Sciences, Division of Materials Sciences and Engineering, under contract DE-AC02-76SF00515. N.R.W. is grateful for the Stanford Interdisciplinary Graduate Fellowship. A.J. thanks the Stanford Department of Chemistry for support through the William S. Johnson award. L.L. acknowledges support by the Bavarian State Ministry of Science and the Arts through the Collaborative Research Network Solar Technologies go Hybrid (SolTech), the Elite Network Bavaria, and the German Research Foundation (DFG) through SFB840 B7 and through computational resources provided by the Bavarian Polymer Institute (BPI). This research used resources of the Advanced Light Source, which is a DOE Office of Science User Facility under contract no. DE-AC02-05CH11231. High-pressure PXRD data were collected at beamline 12.2.2 at the Advanced Light Source (ALS). The high-pressure facilities at the ALS are supported by COMPRES under NSF Cooperative Agreement EAR 11-57758. The authors gratefully acknowledge Dr. Martin Kunz, Dr. Christine Beavers, and Mr. Andrew

Doran at the ALS for assistance with PXRD studies. They thank Dr. Zhenxian Liu for experimental assistance with high-pressure optical absorption measurements. High-pressure vis−IR experiments were performed at beamline 22-IR-1 at the National Synchrotron Light Source II (NSLS-II). The Infrared Laboratory is supported by COMPRES, the Consortium for Materials Properties Research in Earth Sciences under NSF Cooperative Agreement EAR 1606856 and the DOE/National Nuclear Security Administration under Grant DE-NA-0002006, Carnegie DOE Alliance Center (CDAC). NSLS-II is supported by the DOE Office of Science under Contract No. DESC0012704. The authors also thank Samuel Girdzis for experimental assistance and Alexander Su for helpful discussions.

REFERENCES

(1) Wolf, N. R.; Connor, B. A.; Slavney, A. H.; Karunadasa, H. I. Doubling the Stakes: The Promise of Halide Double Perovskites. *Angew. Chem., Int. Ed.* **2021**, *60*, 16264.
(2) Slavney, A. H.; Leppert, L.; Saldivar Valdes, A.; Bartesaghi, D.; Savenije, T. J.; Neaton, J. B.; Karunadasa, H. I. Small-Band-Gap Halide Double Perovskites. *Angew. Chem., Int. Ed.* **2018**, *57*, 12765.
(3) Kröger, F. A.; Vink, H. J.*Solid State Physics*, Seitz, F.; Turnbull, D., Eds.; Academic Press, 1956; Vol. *3*, p 307.
(4) Jantsch, W.; Wünstel, K.; Kumagai, O.; Vogl, P. Deep levels in semiconductors: A quantitative criterion. *Phys. Rev. B* **1982**, *25*, 5515.
(5) Vogl, P.*Advances in Electronics and Electron Physics*, Hawkes, P. W., Ed.; Academic Press, 1984; Vol. *62*, p 101.
(6) Freysoldt, C.; Grabowski, B.; Hickel, T.; Neugebauer, J.; Kresse, G.; Janotti, A.; Van de Walle, C. G. First-principles calculations for point defects in solids. *Rev. Mod. Phys.* **2014**, *86*, 253.
(7) Stradling, R. A.*Festkörperprobleme 25*, Grosse, P., Ed.; Springer: Berlin, Heidelberg, 1985; p 591.
(8) Errandonea, D.; Segura, A.; Manj n, F. J.; Chevy, A. Transport measurements in InSe under high pressure and high temperature: shallow-to-deep donor transformation of Sn related donor impurities. *Semicond. Sci. Technol.* **2003**, *18*, 241.
(9) Hsu, L.; McCluskey, M. D.; Haller, E. E. Pressure dependence of donor excitation spectra in AlSb. *Phys. Rev. B* **2003**, *67*, No. 035209.
(10) Samara, G. A.; Barnes, C. E. Pressure dependence of impurity levels in semiconductors: The deep gold acceptor level and shallow donor and acceptor levels in silicon. *Phys. Rev. B* **1987**, *35*, 7575.
(11) Keller, R.; Fenner, J.; Holzapfel, W. B. The Resistivity of Mixed Valence Compound $Cs_2Au_2Cl_6$ at High Pressure and Low Temperatures. *Mater. Res. Bull.* **1974**, *9*, 1363.
(12) Denner, W.; Schulz, H.; D'Amour, H. The influence of high hydrostatic pressure on the crystal structure of cesium gold chloride ($Cs_2Au^{I}Au^{III}Cl_6$) in the pressure range up to 52 × 10^8 Pa. *Acta Crystallogr., Sect. A: Cryst. Phys., Diffr., Theor. Gen. Crystallogr.* **1979**, *35*, 360.
(13) Jaffe, A.; Lin, Y.; Karunadasa, H. I. Halide Perovskites under Pressure: Accessing New Properties through Lattice Compression. *ACS Energy Lett.* **2017**, *2*, 1549.
(14) Li, Q.; Zhang, L.; Chen, Z.; Quan, Z. Metal halide perovskites under compression. *J. Mater. Chem. A* **2019**, *7*, 16089.
(15) Shi, Y.; Zhou, Y.; Ma, Z.; Xiao, G.; Wang, K.; Zou, B. Structural regulation and optical behavior of three-dimensional metal halide perovskites under pressure. *J. Mater. Chem. C* **2020**, *8*, 12755.
(16) Holland, M. G.; Paul, W. Effect of Pressure on the Energy Levels of Impurities in Semiconductors. I. Arsenic, Indium, and Aluminum in Silicon. *Phys. Rev.* **1962**, *128*, 30.
(17) Nathan, M. I.; Paul, W. Effect of Pressure on the Energy Levels of Impurities in Semiconductors. II. Gold in Silicon. *Phys. Rev.* **1962**, *128*, 38.
(18) Holland, M. G.; Paul, W. Effect of Pressure on the Energy Levels of Impurities in Semiconductors. III. Gold in Germanium. *Phys. Rev.* **1962**, *128*, 43.
(19) Kumagai, O.; Wünstel, K.; Jantsch, W. Deep traps in GaAs under hydrostatic pressure. *Solid State Commun.* **1982**, *41*, 89.
(20) Hutson, A. R.; Jayaraman, A.; Coriell, A. S. Effects of High Pressure, Uniaxial Stress, and Temperature on the Electrical Resistivity of *n*-GaAs. *Phys. Rev.* **1967**, *155*, 786.
(21) Goñi, A. R.; Syassen, K.*Semiconductors and Semimetals*, Tadeusz, S.; William, P., Eds.; Elsevier: Amsterdam, 1998; Vol. *54*, p 247.
(22) Keyes, R. W.*Semiconductors and Semimetals*, Willardson, R. K.; Beer, A. C., Eds.; Elsevier, 1968; Vol. *4*, p 327.
(23) Ghosh, D.; Aziz, A.; Dawson, J. A.; Walker, A. B.; Islam, M. S. Putting the Squeeze on Lead Iodide Perovskites: Pressure-Induced Effects To Tune Their Structural and Optoelectronic Behavior. *Chem. Mater.* **2019**, *31*, 4063.
(24) Kong, L.; Liu, G.; Gong, J.; Hu, Q.; Schaller, R. D.; Dera, P.; Zhang, D.; Liu, Z.; Yang, W.; Zhu, K.; Tang, Y.; Wang, C.; Wei, S.-H.; Xu, T.; Mao, H.-K. Simultaneous band-gap narrowing and carrier-lifetime prolongation of organic−inorganic trihalide perovskites. *Proc. Natl. Acad. Sci. U.S.A.* **2016**, *113*, 8910.
(25) Liu, G.; Kong, L.; Gong, J.; Yang, W.; Mao, H.-K.; Hu, Q.; Liu, Z.; Schaller, R. D.; Zhang, D.; Xu, T. Pressure-Induced Bandgap Optimization in Lead-Based Perovskites with Prolonged Carrier Lifetime and Ambient Retainability. *Adv. Funct. Mater.* **2017**, *27*, No. 1604208.
(26) Wang, Y.; Lü, X.; Yang, W.; Wen, T.; Yang, L.; Ren, X.; Wang, L.; Lin, Z.; Zhao, Y. Pressure-Induced Phase Transformation, Reversible Amorphization, and Anomalous Visible Light Response in Organolead Bromide Perovskite. *J. Am. Chem. Soc.* **2015**, *137*, 11144.
(27) Lü, X.; Wang, Y.; Stoumpos, C. C.; Hu, Q.; Guo, X.; Chen, H.; Yang, L.; Smith, J. S.; Yang, W.; Zhao, Y.; Xu, H.; Kanatzidis, M. G.; Jia, Q. Enhanced Structural Stability and Photo Responsiveness of $CH_3NH_3SnI_3$ Perovskite via Pressure-Induced Amorphization and Recrystallization. *Adv. Mater.* **2016**, *28*, 8663.
(28) Jaffe, A.; Lin, Y.; Beavers, C. M.; Voss, J.; Mao, W. L.; Karunadasa, H. I. High-Pressure Single-Crystal Structures of 3D Lead-Halide Hybrid Perovskites and Pressure Effects on their Electronic and Optical Properties. *ACS Cent. Sci.* **2016**, *2*, 201.
(29) Jaffe, A.; Lin, Y.; Mao, W. L.; Karunadasa, H. I. Pressure-Induced Metallization of the Halide Perovskite $(CH_3NH_3)PbI_3$. *J. Am. Chem. Soc.* **2017**, *139*, 4330.
(30) Wang, P.; Guan, J.; Galeschuk, D. T. K.; Yao, Y.; He, C. F.; Jiang, S.; Zhang, S.; Liu, Y.; Jin, M.; Jin, C.; Song, Y. Pressure-Induced Polymorphic, Optical, and Electronic Transitions of Formamidinium Lead Iodide Perovskite. *J. Phys. Chem. Lett.* **2017**, *8*, 2119.
(31) Liang, Y.; Huang, X.; Huang, Y.; Wang, X.; Li, F.; Wang, Y.; Tian, F.; Liu, B.; Shen, Z. X.; Cui, T. New Metallic Ordered Phase of Perovskite $CsPbI_3$ under Pressure. *Adv. Sci.* **2019**, *6*, No. 1900399.
(32) Jaffe, A.; Lin, Y.; Mao, W. L.; Karunadasa, H. I. Pressure-Induced Conductivity and Yellow-to-Black Piezochromism in a Layered Cu−Cl Hybrid Perovskite. *J. Am. Chem. Soc.* **2015**, *137*, 1673.
(33) Jaffe, A.; Mack, S. A.; Lin, Y.; Mao, W. L.; Neaton, J. B.; Karunadasa, H. I. High Compression-Induced Conductivity in a Layered Cu−Br Perovskite. *Angew. Chem., Int. Ed.* **2020**, *59*, 4017.
(34) Kojima, N.; Kitagawa, H.; Ban, T.; Amita, F.; Nakahara, M. Semiconductor-to-metal and metal-to-metal transitions in the three-dimensional mixed-valence compound $Cs_2Au_2I_6$ under high pressures. *Solid State Commun.* **1990**, *73*, 743.
(35) Kojima, N.; Kitagawa, H.; Ban, T.; Amita, F.; Nakahara, M. Behaviour of the electrical conductivity of the three-dimensional mixed-valence compounds $Cs_2Au_2X_6$ (X=Cl, Br, I) under high pressures. *Synth. Met.* **1991**, *42*, 2347.
(36) Zhao, X. G.; Yang, D.; Sun, Y.; Li, T.; Zhang, L.; Yu, L.; Zunger, A. Cu-In Halide Perovskite Solar Absorbers. *J. Am. Chem. Soc.* **2017**, *139*, 6718−6725.
(37) Zhang, L.; Fang, Y.; Sui, L.; Yan, J.; Wang, K.; Yuan, K.; Mao, W. L.; Zou, B. Tuning Emission and Electron−Phonon Coupling in Lead-Free Halide Double Perovskite $Cs_2AgBiCl_6$ under Pressure. *ACS Energy Lett.* **2019**, *4*, 2975.

https://doi.org/10.1021/jacs.2c08607
J. Am. Chem. Soc. 2022, 144, 20763−20772

(38) Schade, L.; Wright, A. D.; Johnson, R. D.; Dollmann, M.; Wenger, B.; Nayak, P. K.; Prabhakaran, D.; Herz, L. M.; Nicholas, R.; Snaith, H. J.; Radaelli, P. G. Structural and Optical Properties of $Cs_2AgBiBr_6$ Double Perovskite. *ACS Energy Lett.* **2019**, *4*, 299.
(39) Lifshitz, N.; Jayaraman, A.; Logan, R. A.; Card, H. C. Pressure and compositional dependences of the Hall coefficient in $Al_xGa_{1-x}As$ and their significance. *Phys. Rev. B* **1980**, *21*, 670.
(40) Paul, W. Band Structure of the Intermetallic Semiconductors from Pressure Experiments. *J. Appl. Phys.* **1961**, *32*, 2082.
(41) Saxena, A. K. The conduction band structure and deep levels in $Ga_{1-x}Al_xAs$ alloys from a high-pressure experiment. *J. Phys. C: Solid State Phys.* **1980**, *13*, 4323.
(42) Kittel, C.*Introduction to Solid State Physics*, 8th ed.; John Wiley & Sons: Hoboken, NJ, 2005.
(43) Pearson, G. L.; Bardeen, J. Electrical Properties of Pure Silicon and Silicon Alloys Containing Boron and Phosphorus. *Phys. Rev.* **1949**, *75*, 865.
(44) Kohn, W.; Luttinger, J. M. Theory of Donor States in Silicon. *Phys. Rev.* **1955**, *98*, 915.
(45) Li, W.; Sun, Y.-Y.; Li, L.; Zhou, Z.; Tang, J.; Prezhdo, O. V. Control of Charge Recombination in Perovskites by Oxidation State of Halide Vacancy. *J. Am. Chem. Soc.* **2018**, *140*, 15753.
(46) Shi, H.; Du, M.-H. Shallow halogen vacancies in halide optoelectronic materials. *Phys. Rev. B* **2014**, *90*, No. 174103.
(47) Kang, J. Effects of band edge positions on defect structure in lead halide perovskites: A case study on the Br vacancy in $CsPbBr_3$. *Phys. Rev. Mater.* **2020**, *4*, No. 085405.
(48) Li, T.; Zhao, X.; Yang, D.; Du, M.-H.; Zhang, L. Intrinsic Defect Properties in Halide Double Perovskites for Optoelectronic Applications. *Phys. Rev. Appl.* **2018**, *10*, No. 041001.
(49) Cohen, A. V.; Egger, D. A.; Rappe, A. M.; Kronik, L. Breakdown of the Static Picture of Defect Energetics in Halide Perovskites: The Case of the Br Vacancy in $CsPbBr_3$. *J. Phys. Chem. Lett.* **2019**, *10*, 4490.
(50) Slavney, A. H.; Connor, B. A.; Leppert, L.; Karunadasa, H. I. A pencil-and-paper method for elucidating halide double perovskite band structures. *Chem. Sci.* **2019**, *10*, 11041.
(51) Yin, W.-J.; Wei, S.-H.; Al-Jassim, M. M.; Yan, Y. Origin of the diverse behavior of oxygen vacancies in ABO_3 perovskites: A symmetry based analysis. *Phys. Rev. B* **2012**, *85*, No. 201201.
(52) Linderälv, C.; Lindman, A.; Erhart, P. A Unifying Perspective on Oxygen Vacancies in Wide Band Gap Oxides. *J. Phys. Chem. Lett.* **2018**, *9*, 222.
(53) Ball, J. M.; Petrozza, A. Defects in perovskite-halides and their effects in solar cells. *Nat. Energy* **2016**, *1*, 16149.
(54) Walsh, A.; Zunger, A. Instilling defect tolerance in new compounds. *Nat. Mater.* **2017**, *16*, 964.
(55) Euvrard, J.; Yan, Y.; Mitzi, D. B. Electrical doping in halide perovskites. *Nat. Rev. Mater.* **2021**, *6*, 531.
(56) Senocrate, A.; Moudrakovski, I.; Kim, G. Y.; Yang, T.-Y.; Gregori, G.; Grätzel, M.; Maier, J. The Nature of Ion Conduction in Methylammonium Lead Iodide: A Multimethod Approach. *Angew. Chem., Int. Ed.* **2017**, *56*, 7755.
(57) Brandt, R. E.; Stevanović, V.; Ginley, D. S.; Buonassisi, T. Identifying defect-tolerant semiconductors with high minority-carrier lifetimes: beyond hybrid lead halide perovskites. *MRS Commun.* **2015**, *5*, 265.
(58) Brandt, R. E.; Poindexter, J. R.; Gorai, P.; Kurchin, R. C.; Hoye, R. L. Z.; Nienhaus, L.; Wilson, M. W. B.; Polizzotti, J. A.; Sereika, R.; Žaltauskas, R.; Lee, L. C.; MacManus-Driscoll, J. L.; Bawendi, M.; Stevanović, V.; Buonassisi, T. Searching for "Defect-Tolerant" Photovoltaic Materials: Combined Theoretical and Experimental Screening. *Chem. Mater.* **2017**, *29*, 4667.
(59) Deng, Z.; Wei, F.; Sun, S.; Kieslich, G.; Cheetham, A. K.; Bristowe, P. D. Exploring the properties of lead-free hybrid double perovskites using a combined computational-experimental approach. *J. Mater. Chem. A* **2016**, *4*, 12025.
(60) Delor, M.; Slavney, A. H.; Wolf, N. R.; Filip, M. R.; Neaton, J. B.; Karunadasa, H. I.; Ginsberg, N. S. Carrier Diffusion Lengths Exceeding 1 μm Despite Trap-Limited Transport in Halide Double Perovskites. *ACS Energy Lett.* **2020**, *5*, 1337.
(61) Du, K.-z.; Meng, W.; Wang, X.; Yan, Y.; Mitzi, D. B. Bandgap Engineering of Lead-Free Double Perovskite $Cs_2AgBiBr_6$ through Trivalent Metal Alloying. *Angew. Chem., Int. Ed.* **2017**, *56*, 8158.
(62) Xiao, Z.; Du, K.-Z.; Meng, W.; Wang, J.; Mitzi, D. B.; Yan, Y. Intrinsic Instability of $Cs_2In(I)M(III)X_6$ (M = Bi, Sb; X = Halogen) Double Perovskites: A Combined Density Functional Theory and Experimental Study. *J. Am. Chem. Soc.* **2017**, *139*, 6054.
(63) Maughan, A. E.; Ganose, A. M.; Bordelon, M. M.; Miller, E. M.; Scanlon, D. O.; Neilson, J. R. Defect Tolerance to Intolerance in the Vacancy-Ordered Double Perovskite Semiconductors Cs_2SnI_6 and Cs_2TeI_6. *J. Am. Chem. Soc.* **2016**, *138*, 8453.
(64) Xiao, Z.; Meng, W.; Wang, J.; Yan, Y. Thermodynamic Stability and Defect Chemistry of Bismuth-Based Lead-Free Double Perovskites. *ChemSusChem* **2016**, *9*, 2628.
(65) Xu, J.; Liu, J.-B.; Liu, B.-X.; Huang, B. Intrinsic Defect Physics in Indium-based Lead-free Halide Double Perovskites. *J. Phys. Chem. Lett.* **2017**, *8*, 4391.
(66) Wang, D.; Liang, P.; Dong, Y.; Shu, H.; Wang, L.; Liu, Z. Intrinsic point defects in lead-free organic inorganic hybrid double perovskite (OIHDP) $(MA)_2KBiCl_6$. *Org. Electron.* **2020**, *81*, No. 105668.
(67) Xiao, Z.; Yan, Y.; Hosono, H.; Kamiya, T. Roles of Pseudo-Closed s2 Orbitals for Different Intrinsic Hole Generation between Tl−Bi and In−Bi Bromide Double Perovskites. *J. Phys. Chem. Lett.* **2018**, *9*, 258.
(68) Lan, C.; Zhao, S.; Luo, J.; Fan, P. First-principles study of anion diffusion in lead-free halide double perovskites. *Phys. Chem. Chem. Phys.* **2018**, *20*, 24339.
(69) Slavney, A. H.; Leppert, L.; Bartesaghi, D.; Gold-Parker, A.; Toney, M. F.; Savenije, T. J.; Neaton, J. B.; Karunadasa, H. I. Defect-Induced Band-Edge Reconstruction of a Bismuth-Halide Double Perovskite for Visible-Light Absorption. *J. Am. Chem. Soc.* **2017**, *139*, 5015.
(70) Lindquist, K. P.; Mack, S. A.; Slavney, A. H.; Leppert, L.; Gold-Parker, A.; Stebbins, J. F.; Salleo, A.; Toney, M. F.; Neaton, J. B.; Karunadasa, H. I. Tuning the bandgap of $Cs_2AgBiBr_6$ through dilute tin alloying. *Chem. Sci.* **2019**, *10*, 10620.
(71) Milstein, T. J.; Roh, J. Y. D.; Jacoby, L. M.; Crane, M. J.; Sommer, D. E.; Dunham, S. T.; Gamelin, D. R. Ubiquitous Near-Band-Edge Defect State in Rare-Earth-Doped Lead-Halide Perovskites. *Chem. Mater.* **2022**, *34*, 3759.

https://doi.org/10.1021/jacs.2c08607
J. Am. Chem. Soc. 2022, 144, 20763−20772